Supporting Information

Jaeger et al. 10.1073/pnas.1320890111

SI Materials and Methods

In this section we detail the Soil Water Assessment Tool (SWAT) modeling of the Verde River Basin study area (Table S1) and identify and summarize the hydrologic and climatic data sources included in the modeling. We also describe additional analyses of continuity and connectivity metrics including the Dendritic Connectivity Index (DCI) calculation and report on late 21st century differences in flow continuity and connectivity.

SWAT Modeling Calibration and Performance. We simulated streamflow at a daily time step over a 20-y calibration period and individual 19-y validation and modeled current, forecasted mid-21st century and forecasted late 21st century time periods. A 19–20 y simulation period maximized the available historical data for all of the representative stream gauge stations and climate stations used in the hydrologic model. In addition, this simulation period is considered suitably representative for hydrologic analyses because hydrologic metrics tend to stabilize with >15 y of data (1). All simulations included a 3-y warm-up period before the simulation period. Model performance was evaluated for both the calibration and validation periods at a monthly and daily time step.

Landscape and climate data used in SWAT modeling were obtained from a variety of public access sources (Tables S2–S5) (2). We assigned discharge output locations, referred to as "nodes," at an ∼2-km interval along the Verde River main stem (264 km in total upstream of Horseshoe Reservoir) and 11 of its major tributaries. This 2-km interval distance reflects a reasonable compromise between channel length distances that are ecologically meaningful in terms of habitat connectivity and documented dispersal distances for regional fish species and the range of spatial resolution (30-m elevation and land cover data to 1° forecasted climate data) among the landscape and climate data used in the SWAT modeling. The hydrologic model for the VRB was built and initially parameterized using ArcSWAT (v 2009.3.7 with SWAT2009 v 481) (3), a GIS interface software; calibration was conducted using SWAT-CUP4 and SWAT2012 v 585 (4). All subsequent simulations (e.g., validation and forecasted periods) used SWAT2012 v 585.

We calibrated the SWAT model using a 20-y time period (1968–1987) of 7 US Geological Survey (USGS)-operated stream gauges (3 along the Verde River main stem and 4 in downstream portions of tributaries) and 43 National Climatic Data Center (NCDC)-operated climate stations. This suite of stream gauges and climate stations collectively represent the variability of streamflow characteristics of both the tributaries (e.g., from ephemeral to perennial) and along the length of the Verde River main stem as well as the spatial variability of precipitation patterns in this desert climate (Tables S2–S5). We used a multigauge autocalibration procedure using the Particle Swarm Optimization (PSO) algorithm on 21 SWAT parameters that influence discharge (4) (Table S6). This procedure is a preferred optimization method because it is found to generate more accurate results in fewer model iterations (5). For each stream gauge, the calibration procedure identified SWAT parameter values for contributing subbasins to that gauge, which result in the best fit between simulated and measured streamflow. A best fit goal for each iteration was based on the Nash–Sutcliffe coefficient of efficiency parameter (NSE; maximum value of 1 indicates 1:1 simulated:observed fit). The calibration procedure ceased after the specified best fit goal (NSE > 0.7) was achieved or after 1,000 iterations, whichever occurred first. Next, the calibrated parameters for individual subbasins that achieved the highest NSE (best parameters) were adjusted to reflect realistic values (e.g., neither negative nor unreasonably high values for hydraulic conductivity nor negative values for channel roughness coefficients). These final best fit parameters then were incorporated into the calibration procedure for the next downstream stream gauge until the final downstream stream gauge was calibrated (Table S7). Basin-wide parameters (Table S6) were incorporated into the calibration of the final downstream gauge to be comprehensively applied to all subbasins within the VRB.

Predictive performance of the SWAT model is evaluated according to a suite of metrics chosen to assess different components of the hydrograph and which illustrate more fully the calibration skill (6, 7). We considered calibration to be complete based on the best combination of evaluation metrics that achieve or approach values considered acceptable as reported in the literature (7–9) (Table S7 and Fig. S1). We specifically targeted NSE (NSE > 0.5), Percent Bias (PBIAS within ± 25%), and standardized root mean square error (RSR < 0.7) metrics. The model was validated using a 19-y time period of 1988–2006, with the exception of Williamson Wash, which was limited to a 5-y validation period (2002–2006). A statistical comparison of daily streamflow indicates that the calibration and validation time periods display similar hydrologic characteristics (10). Approximately 90% of the dataset (12 mo for seven stream gauges) did not show statistical differences in monthly mean, total, and maximum streamflow.

The SWAT model reasonably simulated streamflow response to precipitation. The SWAT model accurately simulated base flow throughout the VRB and skillfully captured individual streamflow events, although peak discharge magnitudes tended to be under simulated for individual events (Table S7 and Fig. S1). In addition, consistent downstream trends and general agreement among adjacent nodes reflect reasonable streamflow routing processes. Only seven nodes dispersed along the main stem and one node in both Sycamore and Granite Creeks (3% of the total of 300 nodes analyzed in the VRB) did not adequately perform streamflow routing processes, which resulted in streamflow values that were more than 1 order of magnitude smaller than both the adjacent upstream and downstream nodes. In these nine cases, we removed these nodes from the analysis and replaced them with assigned streamflow values that were the computed average of the immediately upstream and downstream node for each day of the simulation period.

Base flow in the VRB is partially supported by groundwater input from two regional aquifers (11, 12). Although climate-induced impacts to groundwater systems are expected, the direction and magnitude of change remain poorly understood (13) and thus are difficult to formally integrate into the hydrologic modeling. We report on climate-induced changes in precipitation runoff patterns, which focus on surface and near-surface hydrologic processes. We do not include an evaluation of climate change response to aquifer water resources with the understanding that potential changes to groundwater may be overshadowed by impacts associated with ongoing groundwater extraction (14).

Modifications to SWAT Model to Account for Forecasted CO_2 Concentrations. The SWAT model used for all five simulation periods was a modified version to account for adjustments in evapotranspiration processes under elevated CO_2 concentrations (detailed in ref. 15) as a function of different vegetation types. CO_2 concentrations for each simulation period are based on

either mean concentrations as reported by the Mauna Lao Observatory (e.g., 330 and 360 ppm for calibration and validation periods, respectively) or projected values under RCP8.5. We used 489 ppm for midcentury CO_2 concentration and 800 ppm as a late century CO_2 concentration with the understanding that the forecasted 1,370 ppm is not expected to occur until the end of the late century simulation period.

Precipitation and Temperature Comparison Between Current and Future Periods. We used forecasted precipitation and average temperate data from a multimodel mean (mmm) analysis that included 16 global circulation models (GCMs, 16-mmm) at 1° by 1° spatial resolution and a monthly time step (2). Mean climate data from the 16 GCMs (Tables S2–S5) were downscaled using a proportional change factor (CF) approach in which observed data were multiplied by a time- and station-dependent constant factor to generate a daily synthetic record that corresponds to the modeled monthly climatic patterns (16–18). Thus, for the precipitation record, in each of the 19-y time periods under consideration,

$$P_k^{(\mathrm{adj})}(t) = \mathrm{CF}_k(t) \times P_k^{(\mathrm{obs})}(t), \qquad \textbf{[S1]}$$

where $P_k^{(\mathrm{obs})}(t)$ is the time record of observed daily precipitation values at climate station k, $\mathrm{CF}_k(t)$ is the time-dependent change factor for station k, and $P_k^{(\mathrm{adj})}(t)$ is the adjusted synthetic precipitation record to be used as downscaled climate data during that period. A similar approach was used for temperature, in which $P_k(t)$ would be replaced by daily mean temperature values.

Change factors were monthly mean proportions between modeled and observed precipitation (or temperature) for each of the three time periods; CFs were computed between the individual 43 climate stations and the appropriate 1° by 1° grid cell of modeled data corresponding to each. For example,

$$\mathrm{CF}_k(\mathrm{month}[t] = \mathrm{Jan}) = \frac{\left\langle P_k^{(\mathrm{GCM})} \right\rangle_{\mathrm{Jan}}}{\left\langle P_k^{(\mathrm{obs})} \right\rangle_{\mathrm{Jan}}}, \qquad \textbf{[S2]}$$

where $\mathrm{CF}_k(\mathrm{month}[t] = \mathrm{Jan})$ is the change factor to be applied to all January daily precipitation data at station k, $\langle P_k^{(\mathrm{obs})} \rangle$ is that station's average observed daily precipitation in January, and $\langle P_k^{(\mathrm{GCM})} \rangle_{\mathrm{Jan}}$ is the 16-mmm average daily precipitation in January at the grid point closest to station k. For temperature data, CFs were computed using ratios of monthly mean temperatures in units of Kelvin. We generated three 19-y CF-adjusted time series that included current (1988–2006), mid-21st century, and late-21st century periods.

The CF approach is a common, computationally straightforward downscaling method that provides climatic variables at space–time scales for use in local watershed models to assess climate impacts (18). It should be noted that for precipitation data, the CF approach preserves the daily climate characteristics of the observed record in terms of number of wet and dry days. Thus, downscaled data in this study reflect forecasted changes in monthly mean precipitation through changes in precipitation event magnitude, rather than the frequency of discrete precipitation events. This approach is reasonable given the lack of forecast information regarding changes of convective precipitation event frequency in the Verde Basin, which is an important climate data downscaling topic that warrants further study.

Monthly values from the 16-mmm reproduce characteristic seasonal precipitation and temperature patterns that are generally consistent with observed monthly values. The 16-mmm reasonably reproduces decreasing precipitation during spring, which increases during the summer monsoon, followed by a dip before increased winter precipitation (Fig. S2). Despite general agreement in patterns, the 16-mmm both overpredicts precipitation by 52% for winter (November–February) and 75% for spring (March–April) and underpredicts precipitation by 33% during the summer monsoon season (Fig. S2). Spatially variable, convective processes account for much of the precipitation in this region, which remains a persistent challenge to effectively model at the watershed scale (2). The 16-mmm underpredicts monthly average temperature in the winter (26%) and overpredicts during the summer monsoon season (10%) (Fig. S2).

Differences in the mean monthly precipitation between the CF-adjusted current period and both midcentury and late century RCP8.5 precipitation for the 43 climate stations included in the SWAT model reflect seasonal trends of the greatest decrease (20%) in precipitation during spring (March–April) and slight decreases (3%) in precipitation during winter (November–February) (Fig. S3). Increased precipitation (7%) is projected for the summer monsoon season (July–September). Similar but amplified differences exist between the current and late century time periods (Fig. S3). Average daily temperatures are forecasted to increase by 2.7 °C by midcentury on average and almost 5 °C over the entire year by late century. The greatest increase is projected during the summer monsoon season (3.0–5.5 °C increase) followed by spring (2.7–4.8 °C increase) and winter (2.4–4.3 °C increase) by both midcentury and late century (Fig. S3). These trends are consistent with other analyses of projected change in this region (2, 19).

We consider the application of the 16-mmm data to CF downscaling a practical and appropriate approach for two reasons. First, the 16-mmm reasonably reproduces seasonal climatic patterns that are similar to the observed record. Second, the 16-mmm demonstrates forecasted changes between current, mid-21st century, and late 21st century precipitation and temperature that are accepted in peer-reviewed literature (2, 19). However, to account for discrepancies between the 16-mmm and observed data, stream drying patterns are assessed between only CF-adjusted time periods. Unadjusted observed data were used only in the SWAT calibration and validation process.

Continuity and Connectivity Metrics. Continuity metrics including the number of zero-flow days, number of zero-flow periods (no units), and duration (days) of zero-flow periods were evaluated annually and seasonally. Seasonal partitioning includes spring (March–June) representing the dominant reproductive (spawning) period for resident fish, the summer monsoon (July–September) coinciding with the period after summer low-flow conditions and representing a period of rapid recolonization into previously dry stream channels, and winter (November–February) season representing network-wide redistribution of resources and prespawning fish migrations during periods of highest hydrologic connectivity. In the American Southwest, the climate during October is characteristically different from both the monsoon and winter seasons; consequently, we do not include October in calculations for either of these seasons but do include the month in the annual (overall) calculations.

Overall and seasonal mean differences in flow continuity metrics between CF-adjusted current and future simulation periods are presented for the Verde River main stem, 11 tributaries, and network-wide (Table S8). Values were computed by first taking differences between midcentury and late century mean zero-flow metrics and current mean zero-flow metrics across all nodes within a river segment (e.g., main stem or individual tributary). Zero-flow metrics include mean zero-flow days, periods, and period durations. Means of differences in zero-flow metrics were then computed across all nodes within the river segment. Increases in stream drying are predicted throughout much of the VRB, particularly during spring followed by summer. Increases in springtime stream drying will drive prominent reductions in connectivity during this season.

Dendritic Connectivity Index. Following Cote et al. (20), we evaluate habitat fragmentation based on daily SWAT simulation output of the Verde River Basin using a DCI, where connectivity is defined as the probability that an individual fish may move between any two points in a river network. The DCI considers the ability of fish to move upstream or downstream between discrete patches of a dendritic system, where each pair of patches has a shared connectivity value, in this case determined by the number and passability of barriers to fish movement between the two. The DCI is essentially an average connectivity (weighted by length) between all possible pairs of patches, given by

$$\mathrm{DCI} = \sum_{i=1}^{n} \sum_{j=1}^{n} \frac{l_i}{L}\frac{l_j}{L} c_{ij} \times 100, \qquad \textbf{[S3]}$$

where n is the total number of individual patches, L is the total dendritic system length, c_{ij} is the connectivity between patches i and j, and l is their respective length. We consider a patch to be any continuous segment of adjacent model nodes with nonzero flow (a spatially continuous wet reach) and evaluate DCI using Eq. **S3**, summing over all possible pairs of wet reaches, for each day of model output.

The connectivity c_{ij} in Eq. **S3** is a function of the number and length of continuous zero-flow reaches, which we consider as temporary dry barriers to fish passage, lying between two wet reaches i and j. It should be noted that these dry fragments represent a nonzero fraction of the total dendritic system length, and on a day of model output in which there is at least one barrier, the system will be less than 100% wet. That is,

$$\sum_{i=1}^{n} \frac{l_i}{L} < 1. \qquad \textbf{[S4]}$$

According to Eq. **S3**, the maximum achievable DCI for that day will be less than 100, even if all $c_{ij} = 1$.

This is a slight extension of the DCI application of Cote et al. (20) in which barriers were treated as fixed and each comprised a node of negligible length between adjacent river segments.

We assume that the passabilities of individual dry reach barriers are independent and further that the passabilities of these barriers in the upstream (p_m^u) and downstream (d_m^d) directions are equal. Under these conditions,

$$c_{ij} = \prod_{m=1}^{M} p_m^u p_m^d = \prod_{m=1}^{M} (p_m)^2, \qquad \textbf{[S5]}$$

where M is the number of dry barriers between wet reaches i and j and p_m is the bidirectional passability of the mth barrier.

We evaluate barrier passability p_m as a function of barrier length l_m in two different ways. The exponential method models p_m as a continuously decaying function of l_m, given by

$$p_m = Ae^{-Bl_m}, \qquad \textbf{[S6]}$$

where A is the passability of a 0-km barrier and B scales the decay of passability as dry reach length increases. This method reflects generalized fish dispersal probabilities. Under the second, threshold method, the passability of any dry barrier is instead a binary function of its length:

$$p_m = \begin{cases} 1 & \text{if } l_m \le \lambda_T \\ 0 & \text{if } l_m > \lambda_T \end{cases}, \qquad \textbf{[S7]}$$

where λ_T is a variable threshold based on reported dispersal distance for a given species. In this case, c_{ij} will equal 1 only if all possible dry barriers between wet reaches i and j are equal to or below the threshold length.

As hydrologic connectivity decreases in response to climate-induced changes to streamflow, fish species will be required to disperse through rewetted channels to recolonize suitable habitats. In recent years a number of studies have supported the idea of heterogeneous movement by fish where populations consist of both stationary and mobile components (21, 22). The stationary component is represented by a high peak in a leptokurtic dispersal kernel and is linked to the concept of fish home range, whereas the mobile component is represented by the fat tail in the leptokurtic dispersal kernel and reflects long-distance dispersal events. Mobile fishes are hypothesized to be responsible for exchange between populations and thus are decisive for genetic exchange and recolonization processes (23). In fact, the movements of such highly mobile and far-dispersing individuals better explain recolonization patterns compared with the overall mean movement of a population (24).

To determine appropriate values of λ_T to be used in the binary threshold method, we used fitted leptokurtic dispersal kernels presented in meta-analysis by Radinger and Wolter (25) to predict the median annual movement rate (km) of mobile individuals for native fish species of the Verde River Basin. By analyzing 160 datasets from 71 studies encompassing 62 fish species and 12 families, Radinger and Wolter (25) demonstrated a strong statistical relationship between movement distance of mobile individuals (σ) and four parameters that included fish morphology (body length, BL; aspect-ratio of the caudal fin, AR), river characteristics (Stahler stream order, SO), and time duration of the study (T):

$$\sigma = -7.48 + 1.45\mathrm{BL} + 0.58\mathrm{AR} + 1.51\mathrm{SO}^{0.5} + \log(0.55\mathrm{T}). \qquad \textbf{[S8]}$$

See table 2 in ref. 25 for specifics on model architecture and predictive performance. Specifically, BL was set to the maximum recorded total body length (mm) for the species (26), AR was derived from photographs of prepared specimens (26), SO was defined as the maximum stream of the VRB or 6, and time was set to 365 d. Notably, estimates of movement rates are most affected by BL and T and vary little according to AR, SO, and family membership. By inputting the maximum BL and maximum SO we take a highly conservative approach that assumes the highest movement rate possible for an individual from each species. Data are reported in Table S9.

To evaluate differences in the sensitivity of native fish species in the VRB to habitat fragmentation, we use the binary threshold method, with varying values of λ_T that reflect species-specific median dispersal distances over a year period for a mobile individual. Our analysis revealed that predicted dispersal distances is highly variable among species, with a range from ~0.5 km for *Poeciliopsis occidentalis* (Gila topminnow) to almost 30 km for *Catostomus insignis* (Sonora sucker) (Table S9). Our premise was that long reaches of continuously dry channels may serve as a temporary barrier for some fish for which dispersal distances are less than the length of that dry length (leading to stranding) but may not be a barrier for fish with dispersal distances exceeding the dry channel length.

Late Century Continuity and Connectivity. Late century (2080–2098) projected changes in continuity and connectivity are similar in direction to midcentury trends but larger in magnitude (Fig. S4). Greater increases in zero-flow days and frequency and duration of zero-flow periods are expected to continue into the late century with associated decreases in connectivity, specifically seasonal declines in DCI in spring (26%) and monsoon (8%) periods. The frequency and mean lengths of dry channel fragments are projected to increase during spring and monsoon seasons (~25% and ~5%), resulting in decreases (6% and 3%) in the proportion of the river network that supports streamflow

during these seasons. We attribute increases in stream drying patterns between the middle and late century to projected continued patterns but larger-magnitude changes in both precipitation and temperature between these time periods (Fig. S3).

1. Kennard M, Mackay SJ, Pusey BJ, Olden JD, Marsh N (2010) Quantifying uncertainty in estimation of hydrologic metrics for ecohydrological studies. *River Res Appl* 26(2): 137–156.
2. Seager R, et al. (2013) Projections of declining surface-water availability for the southwestern United States. *Nat Clim Change* 3(5):482–486.
3. Winchell M, Srinivasan R, Di Luzio M, Arnold JG (2010) *ArcSWAT Interface for SWAT2009, User's Guide* (Grassland, Soil and Water Res Lab, Agric Res Serv, US Dep of Agric, Temple, TX).
4. Abbaspour KC (2011) *SWAT-CUP4: SWAT Calibration and Uncertainty Programs—A User Manual* (Dep of Syst Anal, Integrated Assessment and Model, Eawag, Swiss Fed Inst of Aquat Sci and Technol, Duebendorf, Switzerland).
5. Zhang X, Srinivasan R, Van Liew M (2008) Multi-site calibration of the SWAT model for hydrologic modeling. *Trans ASABE* 51(6):2039–2049.
6. Coffey ME, Workman SR, Taraba JL, Fogle AW (2004) Statistical procedures for evaluating daily and monthly hydrologic model predictions. *Trans ASAE* 47(1):59–68.
7. Moriasi DN, et al. (2007) Model evaluation guidelines for systematic quantification of accuracy in watershed simulations. *Trans ASAE* 50(3):885–900.
8. Gassman PW, Reyes MR, Green CH, Arnold JG (2007) The soil and water assessment tool: Historical development, applications, and future research directions. *Trans ASABE* 50(4):1211–1250.
9. Van Liew MW, Veith TL, Bosch DD, Arnold JG (2007) Suitability of SWAT for the Conservation Effects Assessment Project: Comparison on USDA Agricultural Research Service watersheds. *J Hydrol Eng* 12(2):173–189.
10. Helsel DL, Hirsch RM (2002) *Statistical Methods in Water Resources*, Techniques of Water Resources Investigations Series (US Geol Surv, Washington, DC), Book 4, Chapter A3.
11. Blasch KW, Hoffmann JP, Graser LF, Bryson JR, Flint AL (2006) *Hydrogeology of the Upper and Middle Verde River Watersheds, Central Arizona* (US Geol Surv, Reston, VA), US Geol Surv Sci Invest Rep 2005-5198, 3 plates.
12. Pool DR, Blasch KW, Callegary JB, Leake SA, Graser LF (2011) *Regional Groundwater-Flow Model of the Redwall-Muav, Coconino, and Alluvial Basin Aquifer Systems of Northern and Central Arizona* (US Geol Surv, Reston, VA), US Geol Surv Sci Invest Rep 2010-5180, Version 1.1.
13. Green TR, et al. (2011) Beneath the surface of global change: Impacts of climate change on groundwater. *J Hydrol* 405(3-4):532–560.
14. Garner BD, Pool DR, Tillman FD, Forbes BT (2013) *Human Effects on the Hydrologic System of the Verde Valley, Central Arizona, 1910–2005 and 2005–2110, Using a Regional Groundwater Flow Model* (US Geol Surv, Reston, VA), US Geol Surv Sci Invest Rep 2013-5029.
15. Wu Y, Shuguang L, Abdul-Aziz OI (2012) Hydrological effects of the increased CO_2 and climate change in the Upper Mississippi River Basin using a modified SWAT. *Clim Change* 110(3-4):977–1003.
16. Lettenmaier DP, Wood AW, Palmer RN, Wood EF, Stakhiv EZ (1999) Water resources implications of global warming: A U.S. regional perspective. *Clim Change* 43(3): 537–579.
17. Graham LP, Andréasson J, Carlsson B (2007) Assessing climate change impacts on hydrology from an ensemble of regional climate models, model scales and linking methods—A case study on the Lule River basin. *Clim Change* 81(1):293–307.
18. Teutschbein C, Seibert J (2012) Bias correction of regional climate model simulations for hydrological climate-change impact studies: Review and evaluation of different methods. *J Hydrol* 456:12–29.
19. Ye L, Grimm NB (2013) Modelling potential impacts of climate change on water and nitrate export from a mid-sized, semiarid watershed in the US Southwest. *Clim Change* 120(1-2):419–431.
20. Cote D, Kehler DG, Bourne C, Wiersma YF (2009) A new measure of longitudinal connectivity for stream networks. *Landscape Ecol* 24(1):101–113.
21. Skalski GT, Gilliam JF (2000) Modeling diffusive spread in a heterogeneous population: a movement study with stream fish. *Ecology* 81(6):1685–1700.
22. Rodríguez MA (2002) Restricted movement in stream fish: The paradigm is incomplete, not lost. *Ecology* 83(1):1–13.
23. Albanese B, Angermeier PL, Peterson JT (2009) Does mobility explain variation in colonization and population recovery among stream fishes? *Freshw Biol* 54(7): 1444–1460.
24. Roghair C, Dolloff C (2005) Brook trout movement during and after recolonization of a naturally defaunated stream reach. *N Am J Fish Manage* 25(3):777–784.
25. Radinger J, Wolter C (2013) Patterns and predictors of fish dispersal in rivers. *Fish Fish* 15(3):456–473.
26. Olden JD, Poff NL, Bestgen KR (2008) Trait synergisms and the rarity, extirpation, and extinction risk of desert fishes. *Ecology* 89(3):847–856.

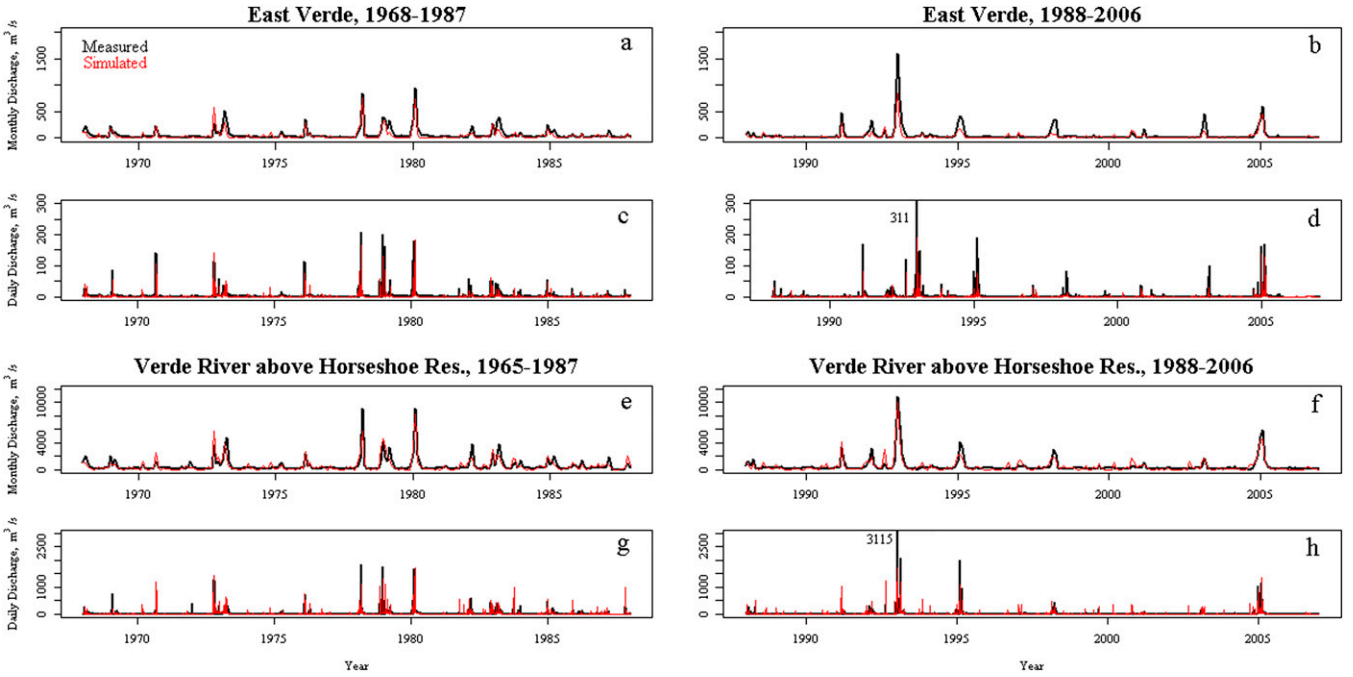

Fig. S1. Graphical evaluation of SWAT simulation for tributary East Verde River (*A*–*D*) and the Verde River main stem above Horseshoe Reservoir (*E*–*H*), which represents streamflow for the entire catchment. Graphical display includes the monthly total (*A*, *B*, *E*, and *F*) and daily (*C*, *D*, *G*, and *H*) discharge for both calibration (*A*, *C*, *E*, and *G*) and validation (*B*, *D*, *F*, and *H*) periods. Numbers within the plotted area refer to discharge values that plot beyond the range of the *y* axis scale.

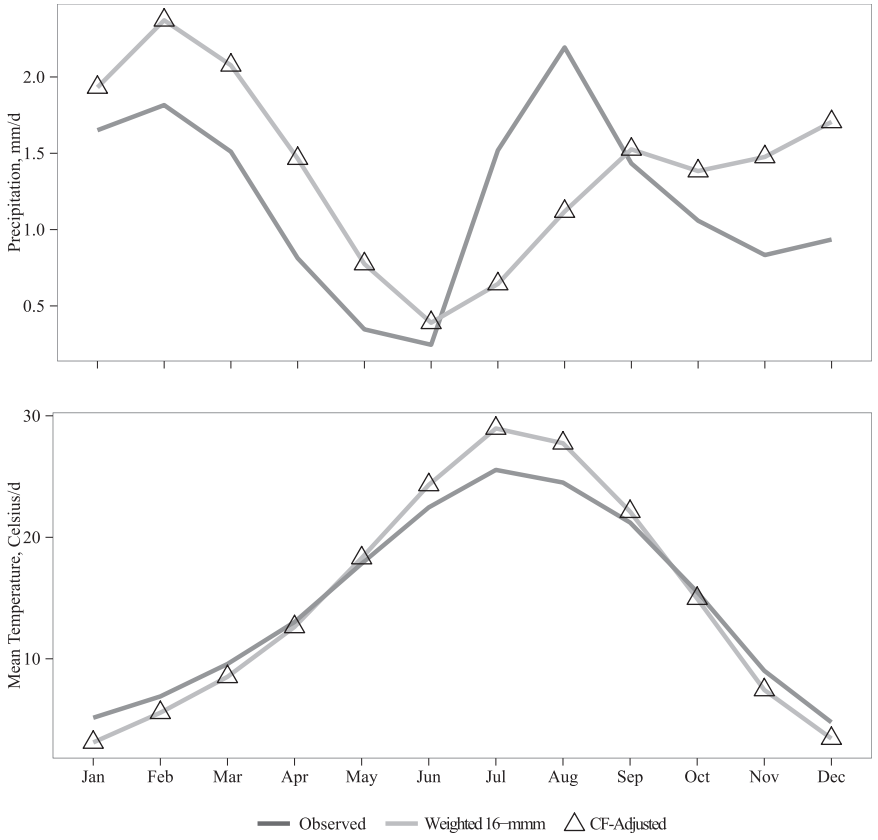

Fig. S2. Mean daily precipitation (*Upper*) and average temperature (*Lower*) by month for observed, 16 GCM multimodel mean (16-mmm), and change factor (CF) adjusted observed values for 1988–2006 time period. Observed values were adjusted using a CF approach to match 16-mmm values.

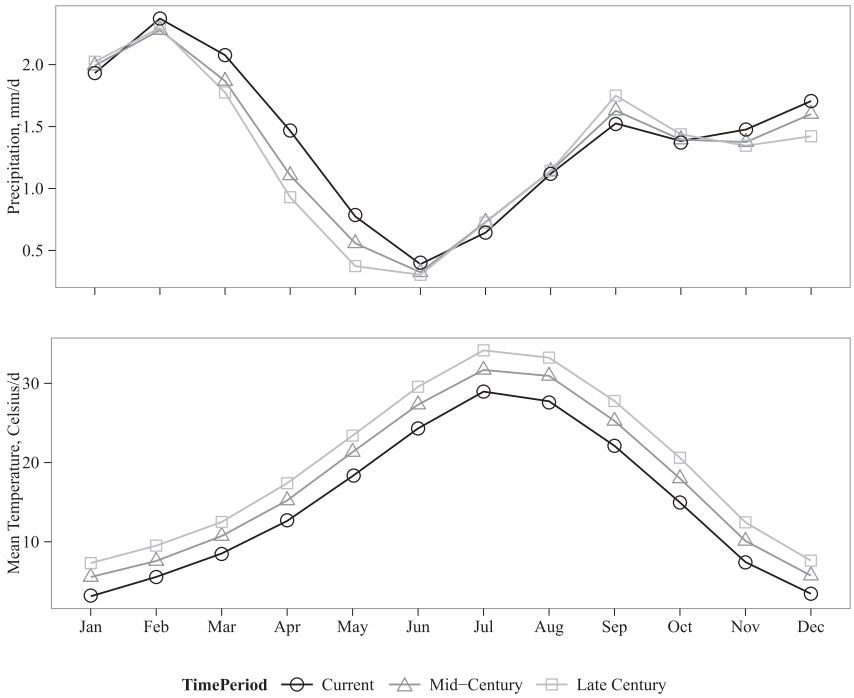

Fig. S3. Mean daily precipitation (*Upper*) and average temperature (*Lower*) by month for the current time period (1988–2006) and the two forecasted time periods (2046–2064 and 2080–2098). Current and forecasted time periods are under the RCP8.5 scenario and synthesized using a change factor method based on a 16 GCM multimodel mean (15) and observed daily data (1988–2006) from 43 climate stations within the VRB. Mean values for each month were computed across the 43 climate stations located within the VRB for all three time periods.

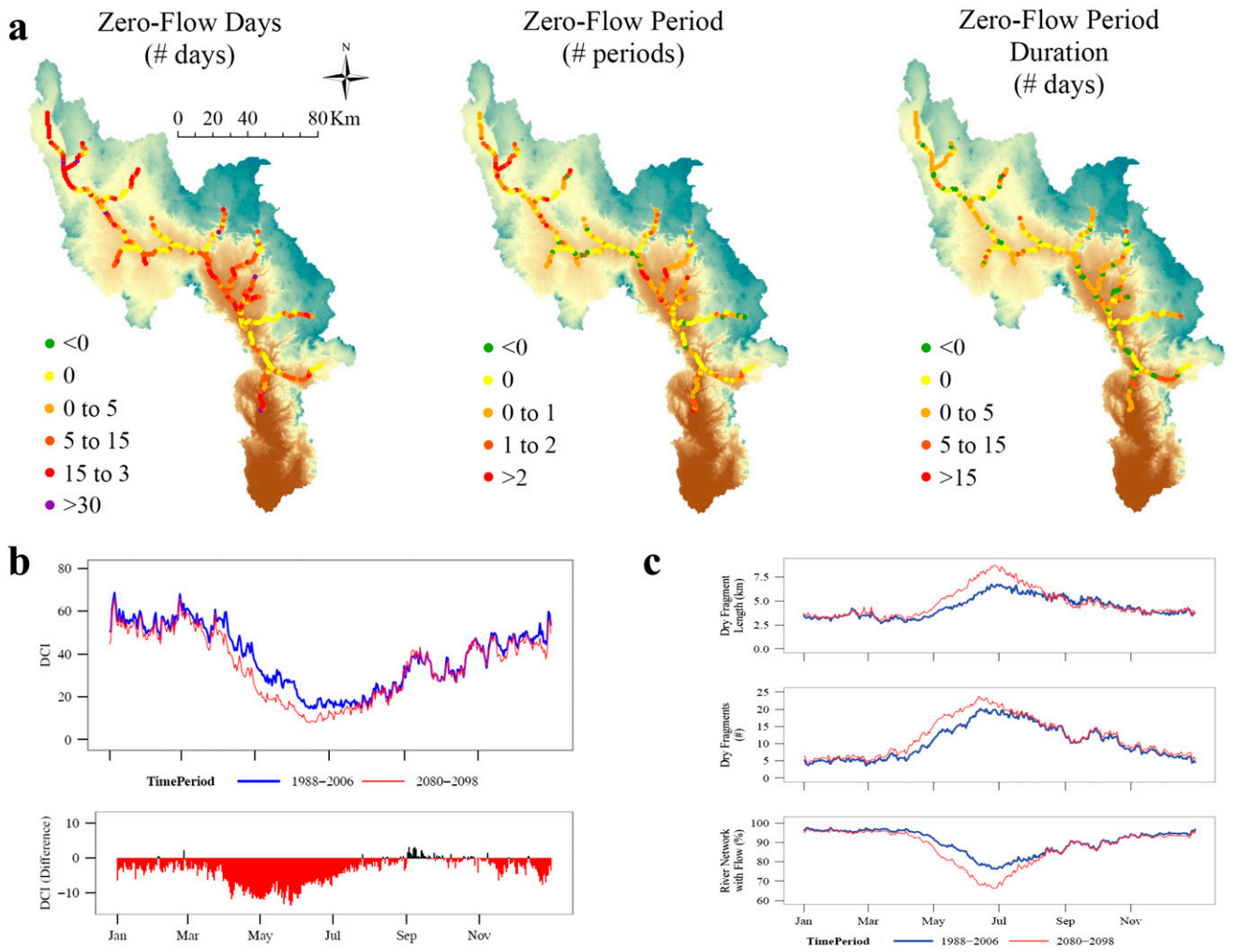

Fig. S4. Differences in flow continuity metrics (mean number of zero-flow days, zero-flow periods, and zero-flow period duration per year) (*A*) and connectivity metrics (DCI using two-parameter exponential decay function) (*B*) and mean dry channel fragment length and frequency (*C*) between current (1988–2006) and late century (2080–2098) time periods. Projected late century differences are similar in direction to midcentury changes in continuity and connectivity metrics but greater in magnitude.

Table S1. Hydrologic characteristics of the Verde River main stem and 11 tributaries included in the study

River	Drainage area, km^2	Channel length, km	Flow regime
Main stem Verde	15,800	264	Perennial
East Verde, RK 34	880	40	Perennial
West Clear Creek, RK 60	656	50	Perennial
Wet Beaver Creek, RK 70	1,165	34	Perennial
Dry Beaver Creek, RK 6*	609	14	Intermittent
Oak Creek, RK 86	883	50	Perennial
Sycamore Creek, RK 114	1,222	32	Perennial
Hell Canyon, RK 132	783	22	Ephemeral
Granite Creek, RK 150	785	6	Ephemeral
Williamson Wash, RK 158	782	26	Intermittent
Partridge Creek, RK 180	1,417	36	Ephemeral
Unnamed Tributary, RK 224	760	24	Ephemeral

The river kilometer (RK, referenced upstream from Horseshoe Reservoir) is the location along the main stem at which each tributary confluences.
*Dry Beaver Creek flows into Wet Beaver Creek rather than directly to the main stem.

Table S2. Public access sources for geographic and hydrologic data used in SWAT modeling

Data type	Resolution	Source	Web address
Elevation	30 m	National Elevation Dataset (NED) from USGS Seamless Data Warehouse	http://seamless.usgs.gov/
Land cover	30 m	National Land Cover Database (NLCD) 2006	www.mrlc.gov/index.php
Soil	1:250,000	USDS-NRCS General Soil Map (STATSGO2)	http://soils.usda.gov/survey/geography/statsgo/
Climate	Daily	USDA Agricultural Research Service (ARS) derived from NOAA	www.ars.usda.gov/Research/docs.htm?docid=19388
Streamflow	Mean daily	USGS National Water Information System	http://waterdata.usgs.gov/nwis/rt

Table S3. List of 16 GCMs used to generate a multimodel mean of current and forecasted climate data (2)

Institute	Climate model ID	RCP8.5 runs
Canadian Centre for Climate Modeling and Analysis (CCCma)	CanESM2	5
National Center for Atmospheric Research (NCAR)	CCSM4	5
Centre National de Recherches Meteorologiques/Centre Europeen de Recherche et Formation Avancees en Calcul Scientifiqu (CNRM-CERFACS)	CNRM-CM5	4
Commonwealth Scientific and Industrial Research Organization in collaboration with the Queensland Climate Change Centre of Excellence (CSIRO-QCCCE)	CSIRO-Mk3-6-0	10
Geophysical Fluid Dynamics Laboratory (NOAA GFDL)	GFDL-ESM2G	1
	GFDL-ESM2M	1
NASA Goddard Institute for Space Studies (NASA GISS)	GISS-E2-R	1
Institute for Numerical Mathematics (INM)	INM-CM4	1
Institut Pierre-Simon Laplace (IPSL)	IPSL-CM5A-LR	4
	IPSL-CM5A-MR	1
Japan Agency for Marine-Earth Science and Technology, Atmosphere and Ocean Research Institute (The University of Tokyo), and National Institute for Environmental Studies	MIROC-ESM	1
	MIROC-ESM-CHEM	1
Atmosphere and Ocean Research Institute (The University of Tokyo), National Institute for Environmental Studies, and Japan Agency for Marine-Earth Science and Technology	MIROC5	3
Max Planck Institute for Meteorology (MPI-M)	MPI-ESM-LR	3
Meteorological Research Institute	MRI-CGCM3	1
Norwegian Climate Centre (NCC)	NorESM1	1

Table S4. List of the seven USGS operated streamflow gauges used for model calibration and validation

USGS streamflow gauge station	Latitude, longitude
Main stem	
Verde River near Paulden (09503700)	34.895°N, 112.342°W
Verde River near Clarkdale (09504000)	34.852°N, 112.065°W
Verde River above Horseshoe Dam (09508500)	34.073°N, 111.716°W
Tributaries	
Williamson Wash (09502800)	34.867°N, 112.613°W
Oak Creek near Cornville (09504500)	34.764°N, 111.890°W
West Clear Creek near Camp Verde (09505800)	34.539°N, 111.693°W
East Verde near Childs (09507980)	34.276°N, 111.638°W

Main stem stream gauge station sequence is in downstream direction; tributary sequence is in the north to south direction.

Table S5. List of the 43 NCDC climate stations used for model calibration and validation

NCDC climate station	Latitude, longitude	Elevation, msl
C023190P	33.6°N, 111.717°W	480
C020632P	33.817°N, 111.65°W	503
C024182P	33.983°N, 111.717°W	616
C021614P	34.35°N, 111.7°W	807
C020625P	34.033°N, 111.367°W	946
C025635P	34.617°N, 111.833°W	969
C022193P	34.75°N, 112.033°W	1,031
C028904P	34.767°N, 112.033°W	1,058
C028653P	33.883°N, 111.833°W	1,122
C028273P	33.917°N, 111.483°W	1,134
C024391P	34.4°N, 111.617°W	1,156
C020670P	34.667°N, 111.717°W	1,164
C026424P	34.9°N, 112.2°W	1,177
C022742P	34.35°N, 111.95°W	1,232
C027708P	34.867°N, 111.767°W	1,286
C023185P	34.417°N, 111.567°W	1,302
C025825P	34.317°N, 111.45°W	1,406
C021654P	34.75°N, 112.45°W	1,448
C028657P	34.617°N, 112.75°W	1,464
C026320P	34.233°N, 111.333°W	1,479
C024453P	34.75°N, 112.117°W	1,509
C029158P	34.933°N, 112.817°W	1,551
C024508P	34.967°N, 111.75°W	1,565
C020487P	35.233°N, 112.483°W	1,568
C020494P	35.217°N, 112.483°W	1,570
C026796P	34.567°N, 112.433°W	1,587
C027720P	35.133°N, 112.917°W	1,598
C027716P	35.333°N, 112.883°W	1,600
C020482P	35.3°N, 112.483°W	1,617
C020490P	35.283°N, 112.467°W	1,623
C026571P	34.383°N, 111.467°W	1,662
C026315P	34.4°N, 111.267°W	1,678
C021193P	34.4°N, 111.367°W	1,681
C021216P	34.8°N, 112.867°W	1,742
C020492P	35.267°N, 112.667°W	1,750
C029572P	34.683°N, 112.167°W	1,830
C025780P	34.933°N, 111.633°W	1,972
C029359P	35.233°N, 112.183°W	2,057
W03103P	35.133°N, 111.667°W	2,132
C023009P	35.167°N, 111.717°W	2,171
C023160P	35.267°N, 111.733°W	2,239
C023828P	34.75°N, 111.417°W	2,280
C025567P	34.7°N, 112.133°W	2,336

Climate stations are listed in geographic sequence collectively from north to south and west to east. Station numbers are in parentheses. Modeled current (1988–2006) and forecasted climate data for the future (2046–2064 and 2080–2098) time period simulations were applied to these climate station locations.

Table S6. SWAT parameters used to calibrate Verde River Basin hydrologic model

Parameter	Process	Range of values	Mean value (SD)	Units	Description
CANMX	Evaporation	0–100	50 (34)	mm H_2O	Maximum canopy storage
EPCO	Evaporation	0–1	0.51 (0.35)	na	Plant uptake compensation factor
ESCO	Evaporation	0–1	0.43 (0.35)	na	Soil evaporation compensation factor
SOL_AWC	Evaporation	0–1	0.54 (0.39)	mm/mm	Available soil water capacity
BIOMIX	Infiltration	0–1	0.46 (0.35)	na	Biological mixing factor
CN2	Runoff	35–100	66 (24)	na	Curve number
SFTMP*	Runoff	−20–20	−1.03	°C	Snowfall temperature
SLSUBBSN	Runoff	10–150	80 (51)	m	Average slope length
SMFMN*	Runoff	0–20	17	mm H_2O/°C-day	Melt factor for snow on December 21
SMFMX*	Runoff	0–20	4	mm H_2O/°C-day	Melt factor for snow on June 21
SMTMP*	Runoff	−20–20	2.16	°C	Snow melt base Temperature
SURLAG*	Runoff	0.04–24	23.16	na	Surface runoff lag coefficient
TIMP*	Runoff	0–1	0.80	na	Snow pack temperature lag factor
TLAPS	Runoff	−10–10	−0.19 (6.13)	°C/km	Temperature lapse rate
CH_K2	Streamflow	0–150, 295, 500[†]	143 (140)	mm/hr	Channel hydraulic conductivity
CH_N2	Streamflow	0.00001–0.5	0.23 (0.18)	na	Channel mannings roughness coefficient
ALPHA_BF	Subsurface	0–1	0.49 (0.36)	days	Base flow alpha factor or recession constant
GW_DELAY	Subsurface	0–500	247 (170)	days	Groundwater delay
GW_REVAP	Subsurface	0.02–0.2	0.11 (0.07)	na	Groundwater "revap" coefficient (water movement from shallow aquifer to the root zone)
GWQMN	Subsurface	0–5,000	3,293 (1,547)	mm H_2O	Threshold depth of water in the shallow aquifer required for return flow to occur
REVAPMN	Subsurface	0–500	6 (4)	mm H_2O	Threshold depth of water in shallow aquifer for "revap" or percolation to deep aquifer to occur

Range of values was applied to 422 individual subbasins that compose the VRB hydrologic model. Mean (SD) values are based on SWAT best parameter values for the 422 individual subbasins.

*Basin-wide parameters are a single calibrated value applied to all subbasins.

[†]CH_K2 maximum values were 150 for the majority of the basin. Upper portions of the basin including Williamson Wash tributary and subbasins draining to the Verde River at Paulden had increased CH_K2 values of 295 and 500, respectively, to reflect the naturally high hydraulic conductance of these ephemeral channels.

Table S7. Calibration and validation evaluation metrics at the monthly and daily time step

	Monthly calibration period (1968–1987)							Monthly validation period (1988–2006)						
Statistic	Verde R. at Paulden	Verde R. at Clarkdale	Verde R. above Horseshoe Dam	Williamson Wash	Oak Creek	West Clear Creek	East Verde	Verde R. at Paulden	Verde R. at Clarkdale	Verde R. above Horseshoe Dam	Williamson Wash	Oak Creek	West Clear Creek	East Verde
RMSE	1.99	6.17	18.31	1.03	2.79	2.47	1.79	2.62	3.98	14.31	1.52	2.30	1.65	2.71
PBIAS	−19	−8	−7	86	−12	−7	−25	−72	−3	−3	43	−16	2	−35
RSR	0.69	0.64	0.50	0.68	0.55	0.62	0.48	0.69	0.38	0.39	0.68	0.48	0.47	0.56
NSE	0.52	0.59	0.75	0.54	0.70	0.62	0.80	0.53	0.85	0.85	0.53	0.77	0.77	0.68
r	0.73	0.78	0.87	0.79	0.84	0.79	0.89	0.84	0.93	0.91	0.74	0.88	0.88	0.91
R^2	0.53	0.61	0.75	0.63	0.71	0.63	0.79	0.71	0.86	0.85	0.55	0.78	0.78	0.84
			Daily calibration period							Daily validation period				
RMSE	5.50	15.67	51.80	2.95	6.93	8.05	4.47	6.87	12.34	45.14	4.65	6.80	5.21	5.71
PBIAS	−19	−8	−4	76	−11	−3	−25	−72	−3	−3	46	−16	−9	−35
RSR	0.82	0.79	0.72	0.71	0.63	0.93	0.56	0.81	0.59	0.63	0.99	0.65	0.68	0.61
NSE	0.33	0.37	0.48	0.50	0.61	0.14	0.69	0.34	0.65	0.60	0.03	0.57	0.53	0.62
r	0.64	0.68	0.75	0.71	0.78	0.50	0.83	0.60	0.81	0.78	0.45	0.76	0.75	0.85
R^2	0.41	0.46	0.56	0.50	0.61	0.25	0.69	0.36	0.65	0.61	0.20	0.57	0.56	0.72

Statistical analysis to evaluate SWAT skill to simulate discharge at seven USGS stream gauges included root mean square error (RMSE), percent bias (PBIAS) (deviation of streamflow discharge expressed as a percent, measures tendency for simulated data to be less than or greater than observed data; optimal = 0, positive values indicate that the model underestimates bias, negative values indicate that the model overestimates bias, acceptable values ± 25%), standardized RMSE (RSR) (indicates error in units of constituents; lower RSR is better model performance, acceptable values < 0.7), Nash–Sutcliffe coefficient of efficiency (NSE) (maximum value of 1 indicates 1:1 simulated:observed fit; acceptable values > 0.5), Pearson correlation coefficient (r) ($-1 \leq r \leq 1$), and coefficient of determination (R^2) ($0 \leq R^2 \leq 1$).

Table S8. Overall and seasonal mean differences in metrics of flow continuity

	Zero-flow days (difference)				Zero-flow periods (difference)				Duration of zero-flow periods (difference)			
Name	Overall	Winter	Spring	Summer	Overall	Winter	Spring	Summer	Overall	Winter	Spring	Summer
Main stem Verde^{P}	6.2	0.6	3.8	1.5	0.5	0.1	0.3	0.2	0.5	1.5	0.2	0.2
East Verde^{P}, RK 34	4.8	0.2	3.6	1.1	0.1	0.0	0.2	0.0	1.9	−0.1	1.0	1.3
West Clear Creek^{P}, RK 60	6.9	−0.2	7.1	1.3	0.4	0.0	0.3	0.2	−0.4	−0.7	1.7	0.2
Wet Beaver Creek^{P}, RK 70	6.3	1.0	3.2	1.8	0.2	0.1	0.1	0.1	0.0	6.7	0.1	1.6
Dry Beaver Creek^{I}, RK 6*	17.9	2.0	10.0	4.5	1.4	0.5	0.7	0.3	0.8	−0.1	1.2	0.5
Oak Creek^{P}, RK 86	11.9	1.6	7.0	2.7	1.1	0.2	0.4	0.5	0.7	0.9	1.2	0.8
Sycamore Creek^{P}, RK 114	7.3	1.6	4.4	0.8	0.8	0.2	0.4	0.2	0.9	1.3	1.0	0.1
Hell Canyon^{E}, RK 132	1.7	0.0	1.1	0.6	0.2	0.0	0.2	0.0	0.1	0.2	−0.6	0.3
Granite Creek^{E}, RK 150	1.4	0.6	0.9	−0.1	0.0	0.0	0.0	0.0	0.1	0.1	0.2	−0.1
Williamson Wash^{I}, RK 158	5.2	0.4	3.7	0.9	0.2	0.0	0.2	0.0	1.1	1.9	0.7	0.5
Partridge Creek^{E}, RK 180	1.0	0.1	0.5	0.3	0.1	0.0	0.1	0.0	0.1	0.0	0.0	0.2
Unnamed tributary^{E}, RK 224	0.0	0.0	0.0	0.0	0.0	0.0	0.0	0.0	0.0	0.0	0.0	0.0
Network-wide	6.1	0.6	4.0	1.4	0.5	0.1	0.3	0.2	0.5	1.2	0.5	0.4

Number of zero-flow days, number of zero-flow periods, and duration (days) of zero-flow periods; between present-day and midcentury simulation periods for the Verde River main stem, 11 tributaries, and network-wide. P, I, and E superscripts indicate present-day perennial, intermittent, and ephemeral hydrologic regime, respectively. RK indicates the river kilometer (referenced upstream from Horseshoe Reservoir) along the Verde River main stem at each major tributary confluence. Positive and negative values indicate an increase or decrease in continuity metric in the future simulation period compared with present-day period, respectively. Differences are taken between modeled current and forecasted midcentury continuity metrics.

Table S9. Native fish species of the Verde River Basin and associated morphological characteristics used to predict median movement distance per year for mobile individuals of the population

Scientific name and common name	Maximum body length, mm	Aspect ratio	Median annual dispersal distance, km
Poeciliopsis occidentalis, Gila topminnow	60	1.54	0.54
Agosia chrysogaster, longfin dace	100	1.29	0.98
Meda fulgida, spikedace	91	1.64	1.04
Rhinichthys osculus, speckled dace	110	1.49	1.25
Catostomus clarkia, desert sucker	330	1.36	5.71
Gila robusta, roundtail chub	430	1.81	10.88
Catostomus insignis, Sonora sucker	800	1.98	29.42

Following ref. 25.